Stability Boundary Analysis for Grid-Following (GFL) and Grid-Forming (GFM) Inverters

Xi Luo, *Student Member, IEEE,* Efstratios Batzelis, *Senior Member, IEEE,*
Abhinav Kumar Singh, *Member, IEEE*

***Abstract*—Studying the dynamics and stability of inverter-driven power systems has become a top priority for grid operators in view of the massive renewable energy deployment. The simplest and most widely used model for stability analysis for such networks is the single-inverter single-bus (SISB) equivalent model. Although quite insightful, SISB models with an L-filter for the inverter suffer from implementation difficulties due to algebraic loops. This paper develops a closed-form SISB model for grid-following (GFL) and grid-forming (GFM) inverters and derives symbolic formulation for the linearized system, which resolves algebraic loops and obtains fast results with uncompromised precision. This model is then used in an N-Dimensional Stability Boundary Tracking (ND-SBT) algorithm, which identifies the stability boundary for GFL and GFM inverters. This is the first method to infer the stability region for an arbitrary number of dimensions in a computationally efficient and software-agnostic manner while preserving accuracy. A detailed sensitivity analysis yields useful findings on the stability impact of individual parameters, while the results are validated using the IEEE 14-bus system.**

***Index Terms*—Renewables integration, Grid-following inverter (GFL), Grid-forming inverter (GFM), stability boundary, small-signal analysis, grid strength.**

NOMENCLATURE

x, x_0	State variables and initial state values.
y_D, y_Q	d-axis, q-axis variables in global DQ frame.
y_d, y_q	d-axis, q-axis variables in local dq frame.
δ	Angle difference between frames.
e_g, v_g, v_m	Grid voltage, PCC point voltage and inverter voltage, resp., in p.u.
α, β, γ	Auxiliary voltage quantities.
i	Grid current.
P, Q	Active and reactive power at PCC.
L_g, L_f	Grid and filter impedance.
P^*, Q^*	Reference active and reactive power.
ω_n, ω_B	System angular speed (frequency) in p.u., and its base-value in rad/s.
ω_c	Cut-off frequency of LPF in rad/s.
$\Delta\omega, \Delta\omega_{filt}$	Deviation between the measured and the reference frequency, and its filtered value.
$\Delta P, \Delta P_{filt}$	Deviation between the measured and the reference power, and its filtered value.
φ_{PLL}	Integral state of PI controller in PLL.
$\varphi_{i_d}, \varphi_{i_q}$	Integral states of current controller.
$\varphi_{v_{gd}}, \varphi_{v_{gq}}$	Integral states of voltage controller.
m_p, m_q	Droop coefficient for active/reactive power.
k_p, k_i	PLL integral and proportional gain.
k_{pv}, k_{iv}	Voltage control integral and proportional gain.
k_{pi}, k_{ii}	Current control integral and proportional gain.

Manuscript received April 14, 2025; revised November 14, 2025; accepted February 09, 2026. This work was supported by the Engineering and Physical Sciences Research Council of UK (EPSRC) as part of the UNIFORM project under Grant EP/Y001575/1. Paper no. TSTE-00495-2025. (*Corresponding author: Xi Luo.*)

Xi Luo, Efstratios Batzelis and Abhinav Kumar Singh are with the School of Electronics and Computer Science, University of Southampton, SO17 1BJ Southampton, U.K. (e-mail: xi.luo@soton.ac.uk; e.batzelis@soton.ac.uk; a.k.singh@soton.ac.uk).

Color versions of one or more of the figures in this article are available online at https://ieeexplore.ieee.org.

Digital Object Identifier

I. INTRODUCTION

INVERTER-BASED resources (IBRs), such as solar plants, wind farms and electric vehicles, have expanded rapidly worldwide in recent years because of their environmental and flexibility benefits. The power electronics that interface these resources to the grid, i.e. the inverter, and their controller play a major role for system stability, especially at high IBR penetrations. Nowadays, most inverters operate in either of two control modes: *grid-following* (GFL) or *grid-forming* (GFM). Although numerous variants exist in each category, a GFL inverter generally behaves as a current source that synchronizes to an established grid, whereas a GFM resource forms its own voltage and frequency. It is now established that both control philosophies have their merits, with GFL usually failing in weak grid and GFM struggling in very stiff systems [1]. Understanding and comparing the stability properties of these controllers at different conditions is currently an active research topic and the focus of this paper.

The most fundamental tool in a stability analysis is the dynamic model of the system, with the simplest version being the single-inverter single-bus (SISB) equivalent. This model considers a single inverter and treats the rest of the power system via its Thévenin equivalent; although simple, this model is often used in state-space formulation to infer the most basic stability properties of the inverter-network interaction [2]–[4]. When the inverter filter is just an inductance L, this model faces implementation difficulties due to an *algebraic loop* formed between the voltage of point of common coupling (PCC) and other variables [5], [6]. Being the midpoint between the filter impedance and grid impedance, the PCC does not have an associated state variable for its voltage; this necessitates solution of a system of several algebraic equations to

TABLE I
STABILITY BOUNDARY METHODS IN THE LITERATURE

Refs	GFL/ GFM	Net. dyn.†	Inv. dyn.‡	Soft. indep.*	Complexity	Dimensions
[1]	Both	✓	✓		Exhaustive search	1
[2], [3]	GFL	✓		✓	Equations	1
[4]	GFM	✓	✓	✓	Equations	1
[16]	GFL	✓	✓		Exhaustive search	2
[17]	GFM	✓	✓		Exhaustive search	2
[18]–[20]	Both	✓	✓		Exhaustive search	2
[21] 'M13'	GFM	✓	✓		Exhaustive search	2
[22], [23]	GFM			✓	Equations	2
[24]	GFL	✓	✓		Exhaustive search	2,3
[25]	GFM	✓		✓	Equations	2,3
[26]	Both	✓	✓		Exhaustive search	1-3
Proposed	**Both**	✓	✓	✓	**Auto**	**N**

†Network dynamics, ‡Inverter internal loop control dynamics, *Software independent

calculate the operating point, i.e. an algebraic loop is formed. This is a well-known problem when a simple L filter is considered, such as (i) when LC or LCL filters are avoided due to resonance and interactions in multi-terminal configurations [7], [8], (ii) for modeling simplicity given similar dynamics for all filter types on the electromechanical time-scale [9], or (iii) just because the filter may be unknown and is approximated as 5%-10% of the system base impedance [10].

Regardless of being a modeling preference or realistic representation, SISB modeling with simple L inverter filter is a necessity but suffers from an algebraic loop. This issue may not pose significant challenges in electromagnetic transient (EMT) simulations, which are accurate but computationally intensive and not well-suited for small-signal or theoretical analysis. However, for dq-based state-space formulations adopted in stability analyses, this algebraic loop increases complexity, slows down simulations, and may even cause execution failure in time-domain studies [11], while also hindering frequency-domain analyses, such as small-signal stability assessment. Quick fixes to this problem are introducing additional state variables, such as a low-pass filter (LPF) in the algebraic path to break the loop [12], [13] or a dummy capacitor at the PCC [14], which both lead to fake eigenvalues (often of high frequency) that may distort dynamics and stability representation as well as increase model complexity. More advanced optimality-based feedback design approaches for solving nonlinear algebraic loops are mentioned in [15]; however, such methods entail significant computational complexity. To this day, there is no closed-form L-filter SISB model without dummy states or algebraic loops for reliable and efficient stability analyses.

The main purpose of such a dynamic model is to infer system stability. There is a plethora of studies that assess small-signal stability in specific cases by identifying the value of a certain parameter that drives the system to instability (e.g. [1]–[4]); for instance, [1] concludes that GFL fails at short circuit ratio (SCR) less than 1.9, while GFM struggles for SCR higher than 9. However, such studies are too case-specific and cannot produce universal findings. A more generic and methodical approach is to determine the *stability boundary* that separates the stable from the unstable region, i.e. the values of parameters that set the system marginally stable [16]–[19]. Extracting the stability boundary is crucial when assessing the conditions or parameters for system instability [24] and has emerged as a widely researched topic lately; a review of the most recent literature [1]–[4], [16]–[26] is summarized in Table I.

An important feature of these methods is controller applicability; most papers focus on either GFL or GFM, with only [1], [18]–[20], [26] supporting both controllers and being able to compare the two. Another critical aspect is the level of detail and accuracy, as all models adopt simplifications that may affect results. For example, [2] focuses only on Phase Locked Loop (PLL) dynamics and neglects all other inverter control loops, whereas [4] ignores the outer power synchronization loop and considers only the internal voltage and current controls. [22] adopts a quasi-static model for the network, while [23] approximates it via Taylor series. Practicality is also a noteworthy implementation factor, i.e. complexity and software dependence. Most methods employ models built in specific software, such as MATLAB/Simulink or PSCAD [18], which are evaluated repeatedly at various parameter combinations to "sample" the stability region and approximate its boundary [16]–[21], [24], [26]; this *exhaustive search* approach entails high computational cost alongside software dependence which limits scope of application. Notably, this exhaustive search can be implemented in either Cartesian coordinates [20]–[23] or polar coordinates [19]. On the other hand, there are some attempts to produce a symbolic representation of the boundary in terms of mathematical equations [2]–[4], [22], [23], which benefit from simple implementation and software independence; although simpler and of wider scope, all such current methods adopt substantial simplifications that render their findings of academic interest only. Last but not least, the majority of these papers are limited to identifying the critical value of one parameter, usually the SCR, (one-dimensional boundary, or 1-D) [1]–[4] or two parameters, usually SCR versus controller gains, (2-D boundary) [16]–[23]. Only a few studies have reached the 3 dimensions [24]–[26], with no method currently available to calculate the multi-dimensional boundary in the general case.

This review indicates that there are still important unanswered questions in the area of SISB modeling and stability assessment. This paper contributes to this topic by:

- Proposing a closed-form SISB model for L-filter GFL and GFM inverters, which resolves the algebraic loop and enjoys fast simulation without a compromise on accuracy.
- Deriving a symbolic formulation for the $\boldsymbol{A}$ matrix of the linearized model, which facilitates eigenvalues calculation and stability assessment.
- Introducing an *N-D Stability Boundary Tracking (ND-SBT)* algorithm, which tracks the multi-dimensional stability boundary in an efficient and software-agnostic manner.
- Providing a structured sensitivity analysis of the stability impact of various parameters, including a new symbolic expression of the minimum SCR for feasible power flow.

The proposed model and algorithm are compared against literature methods initially on the single-bus benchmark and

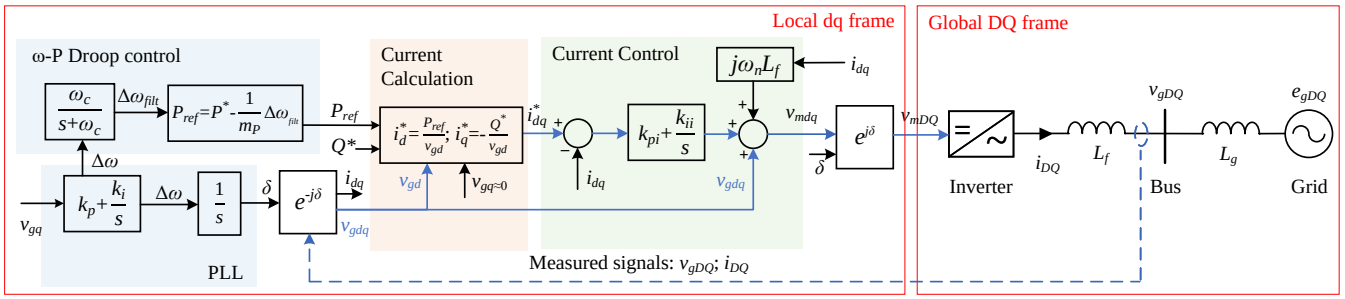

(a)

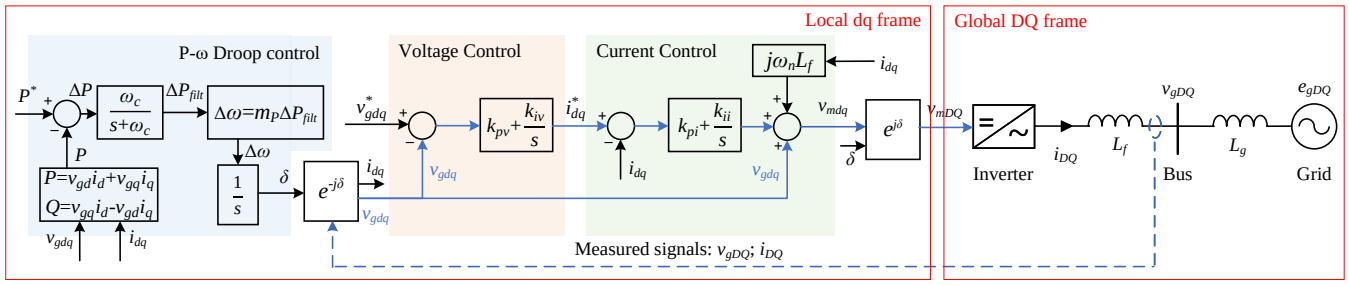

(b)

Fig. 1. Single-Inverter Single-Bus model of a typical (a) grid-following and (b) grid-forming inverter. The algebraic loop is highlighted in blue color.

then validated on the larger IEEE 14-bus system. The rest of this article is organized as follows: Section II first introduces the new closed-form L-filter SISB model, followed by the proposed ND-SBT algorithm in Section III. Section IV assesses the performance of the methods against the state of the art on the single-bus benchmark, while validation on the IEEE 14-bus system is given in Section V. Finally, Section VI summarizes and concludes the paper.

II. Closed-Form SISB Dynamic Model

This section explores the computational challenges of an L-filter SISB model and proposes a reformulation that resolves the algebraic loop. The resulting *closed-form SISB model (CF-SISB)* not only speeds up simulations, but allows for symbolic derivation of the $\boldsymbol{A}$ matrix and straightforward software-independent linear stability analysis. This section explores also initialization of the model and the condition for a feasible power flow.

A. Closed-form state-space model

The SISB system shown in Fig. 1 is the most basic benchmark to understand and compare the stability properties of GFL and GFM controllers. Although the Thévenin representation may not be fully adequate for inverter-driven power systems, it remains a solid starting point for extracting the stability boundary, which is why it has been adopted by all relevant papers in Table I [1]–[4], [16]–[18], [21]–[26]. The line resistance in transmission networks is relatively small (high X/R ratio) and can be safely neglected in stability analysis [1], [3], [26], thus simplifying the grid impedance to an inductance. These assumptions are also reaffirmed in Section V, where the SISB representation of the IEEE 14-bus system yields meaningful and reasonably accurate stability findings.

Typical GFL control with a droop-based frequency response is illustrated in Fig. 1(a). This control structure reflects the increasing needs for primary frequency response by system operators and requires power dispatchability by the primary resource; this flexibility is either naturally available in dispatchable sources (e.g. battery systems) [27] or formed in non-dispatchable sources (e.g. solar and wind farms) via hybridization with energy storage or via keeping headroom, i.e. operating deliberately below capacity for a power margin [28], [29]. The outer loop manages grid synchronization via a PLL and incorporates a frequency-droop ($\omega-P$) control module for primary frequency regulation, while the inner loops convert the power set-points to current commands that eventually drive the inverter output. In contrast, the droop function ($P-\omega$) in GFM scheme (as in Fig. 1(b)) is employed for both synchronization and frequency response, thus actively providing the reference frequency and voltage, which is implemented at the PCC via a voltage and current controller. Numerous variants of these controllers exist in the literature, such as neglecting the frequency low-pass filter or adopting PI controllers in the current calculation stage in GFL, or employing a reactive power-voltage ($Q-V$) droop in the voltage control layer in GFM. Still, Fig. 1 represents possibly the simplest and most widely adopted versions, thus allowing for a fair and meaningful comparison between GFL and GFM.

It is worth noting that the measured voltage v_g at the PCC point is both an input to the control system and an output affected by the control operation. This circular dependency is of algebraic nature, i.e. there is an algebraic path that starts from v_g and ends in v_g referred to simply as *algebraic loop*

and highlighted in blue in the figure. This is due to the absence of a state variable for the PCC voltage, i.e. no capacitor on that node. Please note that this algebraic loop will still appear in alternative control designs, such as PI-based power controllers in the current calculation layer in GFL or Q-V droop in the voltage control layer in GFM, but it is resolved in case of LC or LCL filters on the grid side. However, the necessity for such a model with L-filter for the inverter and Thévenin equivalent for the network has been discussed above.

1) State-space formulation: The non-linear state-space formulation of these models will have the general form of:

$$\dot{\boldsymbol{x}} = g(\boldsymbol{x}, \boldsymbol{u}), \qquad \boldsymbol{y} = h(\boldsymbol{x}, \boldsymbol{u}) \tag{1}$$

where $\boldsymbol{x}, \boldsymbol{u}$ and $\boldsymbol{y}$ are the state, input and output vectors respectively. The GFL model (Fig. 1(a)) has seven states $\boldsymbol{x_{GFL}} = \left[i_D, i_Q, \varphi_{\text{PLL}}, \delta, \Delta\omega_{\text{filt}}, \varphi_{i_\text{d}}, \varphi_{i_\text{q}}\right]^T$, while GFM has eight states $\boldsymbol{x_{GFM}} = \left[i_D, i_Q, \Delta P_{\text{filt}}, \delta, \varphi_{\text{vgd}}, \varphi_{\text{vgq}}, \varphi_{\text{id}}, \varphi_{\text{iq}}\right]^T$, where i_{DQ} is the current, δ is the angle of the inverter frame with respect to the network's global reference frame, φ_{PLL} is the PLL state, $\Delta\omega_{filt}$ and ΔP_{filt} are states from droop control, $\varphi_{v_{gdq}}$ and $\varphi_{i_{dq}}$ are the states from the voltage and current controllers.

For both GFL and GFM, the power circuit is modelled in the global DQ frame, while the inverter control on the local dq frame, as annotated in Fig. 1. Any variable y can be transformed from one frame to another via the angle δ

$$y_{DQ} = y_{dq} e^{j\delta} \Leftrightarrow y_{dq} = y_{DQ} e^{-j\delta} \tag{2}$$

The dynamic model for the network will simply be

$$\dot{i}_D = \frac{v_{gD} - e_{gD}}{L_g} + \omega_n i_Q, \tag{3}$$

$$\dot{i}_Q = \frac{v_{gQ} - e_{gQ}}{L_g} - \omega_n i_D. \tag{4}$$

where e_g and L_g are the Thévenin equivalent grid voltage and inductance, respectively, and w_n is the system nominal frequency taken as 1 p.u. Referring to Fig. 1(a), the set of DAEs governing the dynamics of the GFL control is given by

$$\dot{\varphi_{PLL}} = k_i v_{gq}, \quad \dot{\delta} = k_p v_{gq} + \varphi_{PLL} \tag{5}$$

$$\dot{\Delta\omega_{\text{filt}}} = \omega_c \left(\frac{k_p v_{gq} + \varphi_{PLL}}{\omega_B} - \Delta\omega_{\text{filt}} \right) \tag{6}$$

$$\dot{\varphi_{i_d}} = k_{ii} \left(\frac{P^* - \frac{\Delta\omega_{filt}}{m_p}}{v_{gd}} - i_d \right), \; \dot{\varphi_{i_q}} = k_{ii} \left(-\frac{Q^*}{v_{gd}} - i_q \right), \tag{7}$$

where (5) refers to the proportional–integral (PI) controller of the PLL with state φ_{PLL} and gains k_p, k_i; (6) describes the droop mechanism with droop setting m_p and a low-pass filter (LPF) with state $\Delta\omega_{filt}$ and cut-off frequency ω_c, while ω_B is the system base frequency in rad/s; and (7) formulates the current calculation and PI control with states φ_{idq} and gains k_{pi}, k_{ii}. The superscript $*$ indicates reference variables in this article, e.g., P^* and Q^* are the power set-points.

2) Algebraic loop: The DAEs of the GFL model (2)-(7) comprise states, constants and the algebraic variables v_{gdq}. However, obtaining v_{gdq} is no easy task, as they are part of the aforementioned algebraic loop. Table II gives the variables

TABLE II
SUMMARY OF ALGEBRAIC VARIABLES AND EQUATIONS IN THE LOOP

Part of Model	Equation in GFL	Equation in GFM
Power circuit $v_{mDQ} \rightarrow v_{gDQ}$	$v_{gDQ} = (L_f E_{gDQ} + v_{mDQ} L_g)/(L_f + L_g)$	
DQ to dq $v_{gDQ} \rightarrow v_{gdq}$	$v_{gDQ} = v_{gdq} e^{j\delta}$	
Current calculation $v_{gdq} \rightarrow i^*_{dq}$	$i^*_d \approx P/v_{gd}$, $i^*_q \approx -Q^*/v_{gd}$ Assumption here: $v_{gq} = 0$	$i^*_{dq} = k_{pv}(v^*_{gdq} - v_{gdq}) + \varphi_{v_{gdq}}$
Current control i^*_{dq}, $v_{gdq} \rightarrow v_{mdq}$	$v_{mdq} = v_{gdq} + j\omega_n L_f i_{dq} + k_{pi}(i^*_{dq} - i_{dq}) + \varphi_{i_{dq}}$	
dq to DQ $v_{mdq} \rightarrow v_{mDQ}$	$v_{mdq} = v_{mDQ} e^{-j\delta}$	

and equations involved in that loop, which essentially represent a system of ten algebraic equations with ten unknowns (v_{mDQ}, v_{gDQ}, v_{gdq}, i^*_{dq}, v_{mdq}). Conventionally, this means (i) slower simulations as these ten equations need to be solved numerically in every time step, and (ii) risk of execution failure in case of multiple solutions.

Instead, it is possible to symbolically solve this system of ten equations with ten unknowns, yielding closed-form expressions for the algebraic variables and effectively addressing the algebraic loop. Applying substitution to the equations of Table II for GFL permits reduction of the system to two equations with only v_{gdq} as unknowns:

$$v^2_{gd} = \alpha_d v_{gd} + \beta_d \tag{8}$$

$$v_{gq} = \alpha_q - \beta_q / v_{gd}. \tag{9}$$

where the auxiliary algebraic variables, α_{dq} and β_{dq}, are used for more concise notation and are given by

$$\alpha_{dq} = e_{gdq} + \frac{L_g}{L_f}(\varphi_{i_{dq}} - k_{pi} i_{dq}) + j\omega_n L_g i_{dq}, \tag{10}$$

$$\beta_d = \frac{L_g}{L_f} k_{pi} \left(P^* - \frac{\Delta\omega_{filt}}{m_p} \right), \beta_q = \frac{L_g}{L_f} k_{pi} Q^*. \tag{11}$$

The resulting quadratic equation (8) implies two solutions for $v_{gd1,2} = (\alpha_d \pm \sqrt{(\alpha_d)^2 + 4\beta_d})/2$. For a generator, $P_{ref} = P^* - \Delta\omega_{filt}/m_p$ is non-negative; β_d is also non-negative (see (11)) and the square root will be real (positive argument). This means that the solution with the "$-$" (v_{gd2}) is negative and is thus infeasible and ignored. Therefore, v_{gd} can be given by

$$v_{gd} = \frac{\alpha_d + \sqrt{(\alpha_d)^2 + 4\beta_d}}{2}. \tag{12}$$

Once v_{gd} is calculated from (12), v_{gq} is also explicitly found from (9), and all remaining unknowns can be solved using the algebraic relationships in Table II and substituted back into the state-space model (3)-(7). This allows all unknown algebraic variables to be symbolically expressed as functions of known parameters and state variables (such as L_g, L_f, e_{gdq}, PI gains, i_{dq}, δ, $\Delta\omega_{filt}$, etc.), thereby eliminating the algebraic dependencies and effectively resolving the loop. It is worth emphasizing that without this symbolic manipulation, numerical solution of the algebraic loop may potentially converge to the wrong value for v_{gd}, which will render the solution infeasible and stop execution (simulation crash).

A similar approach is followed for the GFM model, whose

dynamics are governed by (see Fig. 1(b))

$$\Delta\dot{P}_{filt} = \omega_c \left(P^* - i_D v_{gD} - i_Q v_{gQ} - \Delta P_{filt}\right), \tag{13}$$

$$\dot{\delta} = \omega_B m_p \Delta P_{filt}, \tag{14}$$

$$\dot{\varphi_{v_{gd}}} = k_{iv}\left(v_{gd}^* - v_{gd}\right), \dot{\varphi_{v_{gq}}} = k_{iv}\left(v_{gq}^* - v_{gq}\right), \tag{15}$$

$$\dot{\varphi_{i_d}} = k_{ii}\left[k_{pv}\left(v_{gd}^* - v_{gd}\right) + \varphi_{v_{gd}} - i_d\right], \tag{16}$$

$$\dot{\varphi_{i_q}} = k_{ii}\left[k_{pv}\left(v_{gq}^* - v_{gq}\right) + \varphi_{v_{gq}} - i_q\right]. \tag{17}$$

where (13)-(14) refer to the $P-\omega$ droop control that involves state ΔP_{filt}; (15) denotes the voltage controller with states $\varphi_{v_{gdq}}$ and gains k_{pv}, k_{iv}; and (16)-(17) describe the current controller. Evaluating these DAEs requires knowledge of v_{gdq}, which implies again solution of a system of ten equations with ten unknowns as given in Table II for GFM. Here, substitution and manipulation result in a single solution given by

$$v_{gdq} = \frac{L_f(e_{gdq}+j\omega_n L_f i_{dq}) + L_g[k_{pi}(k_{pv}v_{gdq}^* + \varphi_{v_{gdq}} - i_{dq}) + \varphi_{i_{dq}}]}{L_f + L_g k_{pv} k_{pi}}. \tag{18}$$

Similarly, as indicated by (18), the unknown algebraic variables in GFM can be represented using known parameters and state variables, and substituted back into the DAEs to complete the closed-form representation.

3) Complete closed-form GFL and GFM models: The complete GFL model involves 7 differential equations (3)-(7), in which v_{gdq} is found by evaluating (10)-(11), (12) and (9) in that order. The GFM model comprises 8 differential equations (3)-(4) and (13)-(17) and algebraic equation (18) for v_{gdq}.

B. Model Initialization and Linearization

1) Initialization: For the steady-state operating point x_0, the states of the two models can be found by setting the derivative terms of the respective differential equations to zero:

$$\boldsymbol{x_{0,GFL}} = [i_{D0}, i_{Q0}, 0, \delta_0, 0, 0, 0]^{\mathrm{T}} \tag{19}$$

$$\boldsymbol{x_{0,GFM}} = [i_{D0}, i_{Q0}, 0, \delta_0, i_{d0}, i_{q0}, 0, 0]^{\mathrm{T}}, \tag{20}$$

where the subscript 0 indicates steady-state values. These vectors can be used for model initialization in simulation and linear analysis, but they require the initial currents i_{DQ0}, i_{dq0} and angle δ_0. These values correspond to the solution of power flow between two voltage sources v_{gDQ0}, e_{gDQ0} through an impedance $j\omega L_g$, given by

$$\begin{cases} P^* + jQ^* = (v_{gD0} + jv_{gQ0})(i_{D0} - ji_{Q0}) \\ v_{gD0} + jv_{gQ0} = (e_{gD} + je_{gQ}) + j\omega_n L_g (i_{D0} + ji_{Q0}) \end{cases} \tag{21}$$

where P^* and Q^* are the power set-points and the infinite bus is treated as the reference node, i.e. $e_{gQ} = 0$. It can be observed that (21) represents a system of four real equations (when expanded in DQ) with four unknowns i_{DQ0} and v_{gDQ0}.

2) Feasibility condition: Applying substitution in (21) yields the following quadratic equation for i_{Q0}

$$i_{Q0}^2 - i_{Q0} \cdot \frac{e_{gD}}{\omega_n L_g} + \left(\frac{P^*}{e_{gD}}\right)^2 - \frac{Q^*}{\omega_n L_g} = 0, \tag{22}$$

which implies two solutions in the form of

$$i_{Q0} = \frac{e_{gD}}{2\omega_n L_g} \pm \sqrt{\left(\frac{e_{gD}}{2\omega_n L_g}\right)^2 + \frac{Q^*}{\omega_n L_g} - \left(\frac{P^*}{e_{gD}}\right)^2}. \tag{23}$$

For real i_{Q0} value and thus feasible power flow, the argument of the square root in (23) needs to be non-negative at all times. This condition gains physical meaning when the SCR definition in the per unit system is employed

$$SCR = \frac{e_g^2}{X_g} = \frac{e_{gD}^2}{\omega_n L_g}, \tag{24}$$

which allows writing the feasibility condition as

$$\frac{1}{4}SCR^2 + Q^* SCR - P^{*2} \geq 0. \tag{25}$$

It is easy to see that (25) holds true when $SCR \geq 2S^* - 2Q^*$ or $SCR \leq -2S^* - 2Q^*$, where $S^* = \sqrt{P^{*2} + Q^{*2}}$ is the inverter apparent power set-point. Since SCR takes only positive values, the latter solution is rejected, resulting finally in

$$SCR \geq SCR_{min} = 2(S^* - Q^*). \tag{26}$$

This is essentially the definition of minimum SCR for feasible power flow, or equally the maximum grid impedance for transferring the set power across the line. It is worth noting that (26) applies to both GFL and GFM, as it arises from the power flow fundamentals rather than control actions. This entails that even in GFM mode, a very weak grid with $SCR < SCR_{min}$ will impede the implementation of the power set-points; this essentially introduces a *feasibility boundary* which is often overlooked in stability analyses in the literature. For the sake of clarity, a GFM inverter is able to function in a very weak or even islanded grid as the sole generator, but without realizing the set power transfer across the line.

3) Power flow solution: Subject to the feasibility condition (26), there are two real solutions in (23), between which the smallest is acceptable as detailed in Appendix-A. The final solution of the power flow then becomes

$$i_{D0} = \frac{P^*}{e_{gD}}; \quad v_{gQ0} = \omega_n L_g \frac{P^*}{e_{gD}} \tag{27}$$

$$i_{Q0} = \frac{e_{gD}}{2\omega_n L_g} - \sqrt{\left(\frac{e_{gD}}{2\omega_n L_g}\right)^2 + \frac{Q^*}{\omega_n L_g} - \left(\frac{P^*}{e_{gD}}\right)^2} \tag{28}$$

$$v_{gD0} = \frac{e_{gD}}{2} + \sqrt{\left(\frac{e_{gD}}{2}\right)^2 + \omega_n L_g Q^* - \left(\frac{\omega_n L_g P^*}{e_{gD}}\right)^2}. \tag{29}$$

Therefore, the initial variables i_{DQ0} and v_{gDQ0} can be obtained by substituting the steady-state parameter values (P^*, Q^*, e_{gDQ}, L_g, ω_n), that are readily available. The inverter's frame angle is then found by $\delta_0 = \tan^{-1}(v_{gQ0}/v_{gD0})$, which gives i_{dq0} after frame rotation and completes the initialization of states in (19)-(20).

C. Model Linearization and $\boldsymbol{A}$ matrix

To assess small-signal stability, the aforementioned non-linear state-space models need to be linearized as

$$\dot{\boldsymbol{x}} = \boldsymbol{A}\boldsymbol{x} + \boldsymbol{B}\boldsymbol{u}, \tag{30}$$

where matrix $\boldsymbol{A}$ reflects the system dynamics and is essential for eigenvalue and stability analysis. With the conventional models that contain algebraic loops, the only way to determine

$\boldsymbol{A}$ is via input perturbation and subsequent output measurements [30]. This is essentially numerical approximation of the $\partial g/\partial x$ partial derivatives (see (1)), which is both time-consuming and prone to inaccuracies due to potential measurement errors in complex systems. It also depends on specialized software tools, such as MATLAB/Linearization Toolbox, Wolfram Mathematica, or Python/control library, which limits the scope of such analysis to solely academic.

This paper proposes instead a symbolic derivation of the $\boldsymbol{A}$ matrix by leveraging the closed-form reformulation of the GFL and GFM models. This form enables explicit mathematical expression for each element in $\boldsymbol{A}$, thus providing a detailed analytical representation of the system. The details and full breakdown are given in Appendix-B. With this symbolic formulation, it is straightforward and software-agnostic to evaluate $\boldsymbol{A}$ at any condition by: (i) initializing the model according to Section II-B, (ii) evaluating $\boldsymbol{A}$ via the explicit expressions in Appendix-B, and then (iii) applying linear algebra to calculate the eigenvalues and assess stability, damping and other dynamic properties.

III. Stability Boundary Tracking

Building upon the improved closed-form model, this section introduces an efficient method to capture the multidimensional stability boundary for both GFL and GFM systems, referred to hereinafter as *N-Dimensional Stability Boundary Tracking (ND-SBT)* algorithm. The method is given by the flowcharts of Fig. 2 and Fig. 3, and adopts recursive formulation to support an arbitrary number of dimensions N. In the following, $\boldsymbol{p} = [p_1, p_2, \ldots, p_N]$ is the vector of values of N parameters of interest, selected among the grid parameters $\{L_g,\ L_f,\ e_g\}$ and either GFL parameters $\{m_p,\ f_c,\ k_p,\ k_i\}$ or GFM parameters $\{m_p,\ f_c,\ k_{pv},\ k_{iv}\}$; $\boldsymbol{p_{\min}} = [p_{\min,1}, p_{\min,2}, \ldots, p_{\min,N}]$ and $\boldsymbol{p_{\max}} = [p_{\max,1}, p_{\max,2}, \ldots, p_{\max,N}]$ are the lower and upper parameter bound vectors respectively; $\boldsymbol{\Delta p} = [\Delta p_1, \Delta p_2, \ldots, \Delta p_N]$ is the parameter step size vector; and $\mathcal{B}_N$ represents the N-D stability boundary found by evaluating the function $f(N)$. Please note that this method is for small-signal stability, but the concept can be generalized to other stability analyses after modification. It can also be extended to other implementations such as LC- or LCL-filter models, where only matrix $\boldsymbol{A}$ needs to be updated while the feasibility boundary remains unchanged.

A. Critical Value Identification (1-D Stability Boundary)

Extracting the system eigenvalues λ from the matrix $\boldsymbol{A}$ can directly infer small-signal stability under certain conditions. To assess the stability impact of a certain parameter, it is useful to determine the critical value that drives the system to instability, i.e. the 1-D stability boundary. This task involves calculating the minimum damping ratio ζ among all eigenvalues and finding when it becomes zero.

1) Minimum damping function $\zeta_{min}(\rho)$: The algorithm for obtaining the minimum damping ratio $\zeta_{min}(\rho)$ is illustrated in Fig. 2. For a certain parameter value ρ, the model is initialized according to Section II-B, after which the $\boldsymbol{A}$ matrix can be explicitly derived based on Appendix-B. The eigenvalues λ are

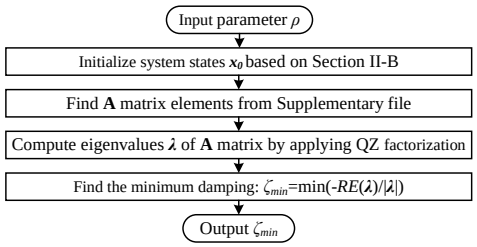

Fig. 2. Flowchart of minimum damping function $\zeta_{min}(\rho)$.

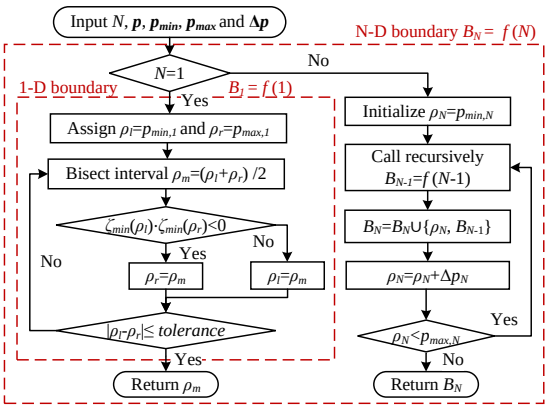

Fig. 3. Flowchart of the N-D Stability Boundary Tracking (ND-SBT) algorithm in recursive formulation $f(N)$.

then calculated from $\boldsymbol{A}$ by applying Generalized Schur (QZ) factorization [31], which allows damping ratio calculation and selection of the minimum value as $\zeta_{min}(\rho)$. It is worth noting that all operations in Fig. 2 are software-agnostic, including $\boldsymbol{A}$ matrix derivation and QZ factorization that is easily implemented in any programming language.

2) Critical value identification: The flowchart of Fig. 3 gives the full ND-SBT algorithm, which in one dimension, $N = 1$, entails solving $\zeta_{min}(\rho) = 0$, i.e. finding the critical parameter ρ_m that drives the system marginally stable. Since $\zeta_{min}(\rho)$ is a continuous function, it can be solved via the Bisection method [32] so as to avoid derivative calculations as with Newton-like techniques. The proposed algorithm given in the left branch in Fig. 3 involves the standard Bisection steps of initializing the search interval from the parameter bounds $(p_{\min,1}, p_{\max,1})$ and successively halving the interval until a certain tolerance threshold is met. This process returns the 1-D boundary $\mathcal{B}_1 = f(1)$ with logarithmic complexity $O(\log n)$, as opposed to the conventional sensitivity analysis of linear complexity $O(n)$ found in the literature [33].

B. ND-SBT Algorithm

The multidimensional boundary $\mathcal{B}_N$ represents the combination of values of the N parameters that drive the system marginally stable. This is mathematically formulated as a set

$$\mathcal{B}_N = \{\{\rho_N, \mathcal{B}_{N-1}\} \mid \rho_N \in (p_{\min,N}, p_{\max,N}) \wedge\ \mathcal{B}_{N-1} = f(N-1)\}, \qquad (31)$$

i.e. $\mathcal{B}_N$ is a collection of subsets $\{\rho_N, \mathcal{B}_{N-1}\}$, each relating a ρ_N value with a boundary of lower dimension $\mathcal{B}_{N-1}$.

TABLE III
SYSTEM RATED PARAMETERS

Model	Parameter
Grid & Filter	$\omega_B = 100\pi$ rad/s; $L_f = 0.20$ pu; $e_g = 1$ pu; $P^* = 1$ pu; $Q^* = 0$ pu;
GFL	$m_p = 1\%$; $f_c = 10$ Hz; $k_p = 1.4$; $k_i = 5000$; $k_{pi} = 1.25$; $k_{ii} = 10$;
GFM	$m_p = 5\%$; $f_c = 20$ Hz; $k_{pv} = 5$; $k_{iv} = 250$;$k_{pi} = 1.25$; $k_{ii} = 10$.

Therefore, $\mathcal{B}_1$ contains a single value, e.g. the critical SCR; $\mathcal{B}_2$ represents a collection of data points that is a curve, e.g. the 2-D $m_p - SCR$ relation; $\mathcal{B}_3$ is a collection of curves that is a surface, e.g. the 3-D $f_c - m_p - SCR$ relation and so on.

The ND-SBT algorithm of Fig. 3 produces $\mathcal{B}_N$ recursively, starting from N and successively lowering dimension till $N = 1$ when $\mathcal{B}_1$ is found via bisection. At dimension N, the parameter of interest ρ_N is varied within $(p_{\min,N}, p_{\max,N})$ with a step Δp_N, and for every value the respective lower-dimension boundary $\mathcal{B}_{N-1}$ is found for the $\{\rho_N, \mathcal{B}_{N-1}\}$ subset to be added into $\mathcal{B}_N$ superset. Please note that finding $\mathcal{B}_{N-1}$ entails recursive evaluation of $f(N-1)$, which in turn implies nested call of $f(N-2)$, $f(N-3)$ and so on till $f(1)$.

It is worth emphasizing the benefit of ND-SBT algorithm against the exhaustive search often employed in the literature [16]–[18] (see Table I). Instead of testing all parameter combinations and uniformly sampling the entire multidimensional space, ND-SBT explores only the region around the boundary. This entails considerable computational benefit, as detailed in the following section, alongside software independence and wider scope of application already discussed. This calculation efficiency is of vital importance during off-line boundary calculations in multiple scenarios at the planning stage, but it also enables online applications such as real-time control adaptation to grid conditions based on these boundaries.

IV. CASE STUDIES AND INSIGHTS

This section assesses the efficacy of the proposed closed-form SISB model and ND-SBT algorithm against existing literature evaluated on the infinite bus benchmark of Fig. 1 (parameters in Table III).

A. Closed-form SISB model performance

The performance of the proposed closed-form L-filter SISB model (*CF-SISB*) is compared to the alternative of breaking the algebraic loop via an LPF (*LPF*) (time constant τ varying from $10ns$ to $1ms$) and the default approach of not resolving the algebraic loop at all (*AL*).

1) Model fidelity: Fig. 4 shows the critical eigenvalues of the three models: CF-SISB and AL models coincide, but LPF misrepresents dynamic behavior for high τ values [12], [13]. This is reaffirmed in the large-disturbance time-domain results of Fig. 5, where a high-τ LPF model yields falsely undamped response (Fig. 5(a)) and AL features random disturbances stemming from numerical instability (Fig. 5(b)).

2) Time-domain performance: The simulation performance of the said models is evaluated via a variable-step solver in Table IV and a fixed-step solver in Table V. In the former case, the number of simulation steps and execution time (T_{exe}) quantify computational effort, with fewer steps and lower

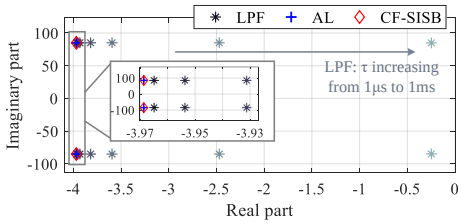

Fig. 4. Comparison of critical eigenvalues.

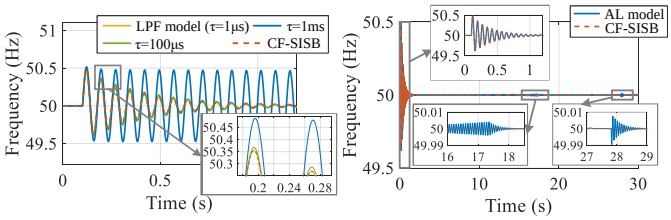

Fig. 5. Time-domain simulation comparison of CF-SISB with (a) LPF and (b) AL models.

T_{exe} implying faster execution. The simulation accuracy is reflected by the RMSE of the simulated frequency signal against the true values, while model stiffness is evaluated from the largest magnitude of the system eigenvalues, where larger eigenvalues indicate increased stiffness and greater numerical difficulty. Table IV shows that LPF usually requires more execution steps than CF-SISB resulting in substantially longer simulation times; lower τ in LPF entails lower modeling error (simulation RMSE) at the cost of larger maximum eigenvalue λ_{max} and model stiffness. On the other hand, AL is the most computationally demanding model, while delivering subpar accuracy because of the numerical instability discussed above.

These findings are further supported by the fixed-step simulations in Table V, which evaluate performance under different time-step settings (in μs). As the time step increases and the simulation time decreases, AL always remains the slowest-running model. For the LPF model, when the time step exceeds the filter time constant, τ, numerical instability occurs and the simulation crashes (giving N/A values). This demonstrates the trade-off between computational efficiency and solver stability in the LPF model, whereas the proposed CF-SISB avoids this issue and maintains shorter simulation times across all tested step sizes.

This analysis shows that time-domain simulations with either AL or LPF are always inferior to CF-SISB in both accuracy, execution time and numerical stability. An LPF model with a small time constant is the second-best option, but it always holds the risk of execution failure even in variable-step settings if the solver fails to properly adjust the time step.

3) Frequency-domain performance: Table VI provides the eigenvalue calculation cost by the three models as the average from about one hundred thousand cases with different parameters $\boldsymbol{p}$. The total execution time is split into the cost of the three main phases of (i) initialization, (ii) linearization, and (iii) eigenvalue calculation. All models share the same code for

TABLE IV
COMPUTATIONAL PERFORMANCE WITH VARIABLE-STEP SOLVER

	Approach	LPF					AL	CF-SISB
	τ (μs)	0.01	0.1	1	10	100	-	-
GFL	No. of steps	11,230	11,037	9,684	14,044	24,217	152,320	7,800
	T_{exe} (s)	1.56	1.46	1.35	2.16	3.63	23.91	0.31
	RMSE (%)	$1.27e^{-6}$	$1.47e^{-6}$	$8.71e^{-6}$	$8.84e^{-5}$	$9.50e^{-4}$	$4.10e^{-4}$	-
	λ_{max}	$1.09e^{8}$	$1.09e^{7}$	$1.09e^{6}$	$1.09e^{5}$	$1.10e^{4}$	$1.95e^{3}$	$1.95e^{3}$
GFM	No. of steps	5,571	5,614	5,563	5,556	815,210	9,894	5,589
	T_{exe} (s)	0.97	0.69	0.71	0.72	92.90	2.37	0.45
	RMSE (%)	$2.11e^{-7}$	$7.39e^{-7}$	$6.72e^{-6}$	$6.73e^{-5}$	$6.90e^{-4}$	$9.40e^{-4}$	-
	λ_{max}	$3.38e^{8}$	$3.38e^{7}$	$3.38e^{6}$	$3.39e^{5}$	$3.46e^{4}$	$4.24e^{2}$	$4.24e^{2}$

TABLE V
EXECUTION TIME WITH FIXED-STEP SOLVER (SIMULATION TIME 10S)

	Time Step (μs)	LPF (τ (μs))			AL	CF-SISB
		1	10	100		
GFL	1	297.50	294.163	289.08	662.98	73.45
	10	N/A	87.63	87.08	112.99	7.06
	50	N/A	N/A	16.32	23.15	2.49
	500	N/A	N/A	N/A	3.04	0.53
GFM	1	N/A	547.81	550.80	957.16	236.63
	10	N/A	N/A	56.58	103.57	25.03
	50	N/A	N/A	11.41	21.16	5.31
	500	N/A	N/A	N/A	1.87	0.45

TABLE VI
AVERAGE EIGENVALUES CALCULATION COST

Model	Execution time (s)			Total time(s)
	Initialization	Linearization	Eigenvalue calculation	
LPF	$1.55e^{-4}$	0.4982	$7.21e^{-5}$	0.4984
AL	$1.48e^{-4}$	0.4906	$6.32e^{-5}$	0.4908
CF-SISB	$9.42e^{-5}$	$2.01e^{-6}$	$9.68e^{-6}$	$1.06e^{-4}$

initialization (Section II-B) and eigenvalue computation (Section III-A), but linearization in LPF and AL is performed via the conventional perturbation approach via the linear analysis tool in MATLAB. These metrics represent the computational cost associated with each stage, allowing a detailed evaluation of performance differences among models. The results indicate that linearization in LPF and AL is the most burdensome step by far, in stark contrast to CF-SISB. This eye-catching difference is not only due to the inferior linearization method, but also due to computational overheads from employing such tools. This highlights the double benefit of symbolic linearization, which alongside software independence delivers 4 orders of magnitude faster execution.

B. Stability Boundaries and ND-SBT performance

The outputs of ND-SBT are discussed and compared to the literature, leading to useful findings on GFL/GFM stability.

1) 1-D, 2-D and 3-D boundary examples: The conventional approach for 1-D stability analysis involves capturing the eigenvalue traces for a varying parameter of interest, e.g. SCR in Fig. 6, and find when they cross the imaginary axis. The ND-SBT algorithm can instead directly infer that GFL becomes unstable for SCR below 2.82 and GFM above 7.55 in Fig. 6 (values in line with literature [1]), thus avoiding the usual graphical trial&error approach.

An indicative 2-D stability boundary, i.e. stability curve, relating m_p with SCR is given in Fig. 7 (a)-(b) for the two controllers. The plots depict how the stability boundary (solid line) and the feasibility boundary (dashed line) split the 2-D

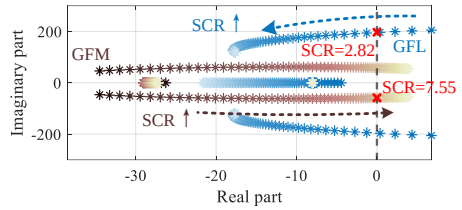

Fig. 6. Traces of low-frequency eigenvalues for varying SCR.

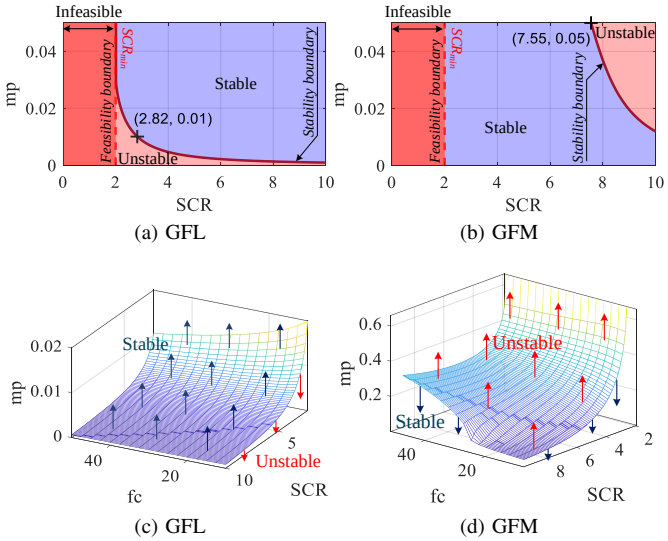

Fig. 7. Examples of stability boundaries in (a)-(b) 2-D, and (c)-(d) 3-D plots.

space into three regions: infeasible (dark red), unstable (light red) and stable (blue). This is particularly important for GFM, whose stable region is evidently constrained by power flow feasibility at very low SCR, a fact often neglected in stability analyses in the literature. It is also worth noting the reverse stability trend of m_p in GFL and GFM: high responsiveness to frequency fluctuation (low m_p) is effortless in GFM, but quite challenging in GFL due to time delays involved.

A 3-D example is also given via the stability surfaces of Fig. 7 (c)-(d) for the relation $f_c - m_p - SCR$ (feasibility surface not shown for legibility). Such plots can be quite informative for parameter tuning as well as stability inference.

2) Sensitivity analysis: A detailed sensitivity analysis on the stability impact of the main parameters is given here via the 2-D plots of Fig. 8. The stability curves (solid lines) of GFL parameters $\{m_p, f_c, k_p, k_i\}$ and GFM parameters $\{m_p, f_c, k_{pv}, k_{iv}\}$ with SCR are shown for varying power factor (PF) (fixed apparent power, different colour) alongside the respective feasibility boundaries (dashed lines). Key findings are summarized in Table VII. For example, m_p has the opposite effect on GFL and GFM stability as already discussed, but low f_c is detrimental for both controllers implying increased time lag that is unfavourable in closed-loop control systems [34]. Interestingly, lagging PF expands the stable and feasible regions in both cases, which agrees with the literature on leading PF causing voltage instability [35] and limiting the acceptable SCR [1].

Although some of these observations are sporadically re-

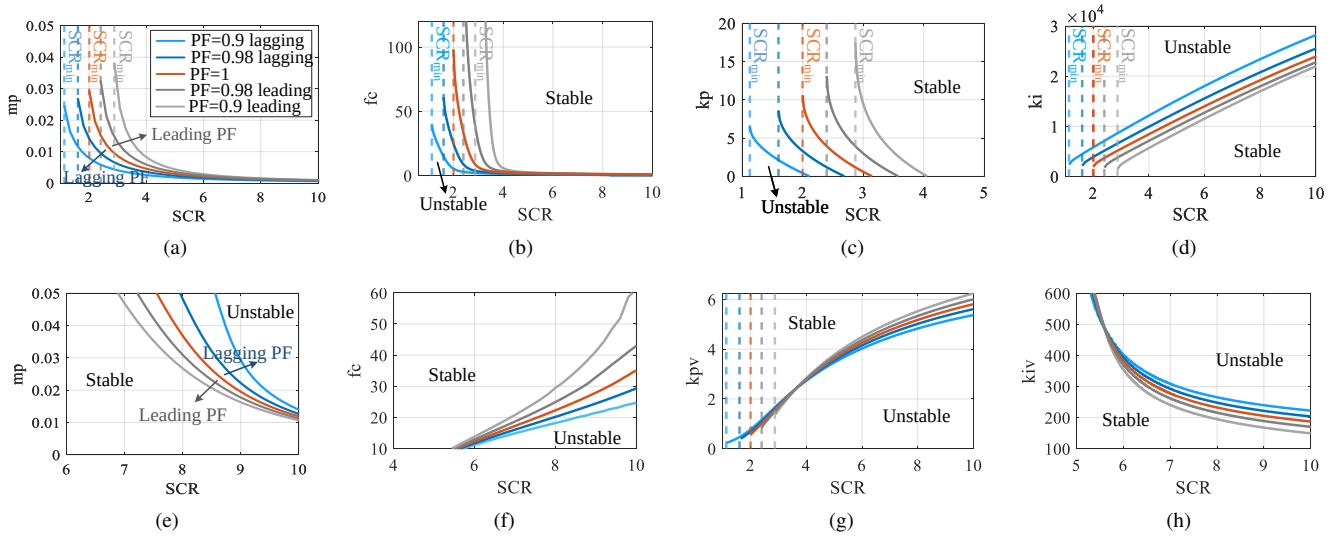

Fig. 8. 2-D stability boundary plots for various parameters vs SCR in (a)-(d) GFL and (e)-(h) GFM. Dashed lines refer to feasibility boundaries, solid lines to stability boundaries and different colours to varying power factor.

TABLE VII
STABILITY IMPACT OF VARIOUS PARAMETERS

Model	Parameter tuning for expanding stability region					
	SCR	m_p	f_c	k_p/k_{pv}	k_i/k_{iv}	PF
GFL	↑	↑	↑	↑	↓	lagging*
GFM	↓	↓	↑	↑	↓	lagging*

↑ Increasing value, ↓ Reducing value, *Feasible region also expands

ported in the literature, prior studies have generally focused on limited conditions or individual parameters. The ND-SBT algorithm provides for the first time methodical quantification and visualization of these trends across multiple parameters and dimensions. This comprehensive mapping enables direct comparison of GFL and GFM behaviors and not only consolidates scattered findings from previous studies but also offers new insights into the fundamental stability mechanisms, such as the GFL and GFM stability duality discussed later.

3) Comparison with literature: The performance of ND-SBT is assessed here against the symbolic boundary representations of the literature [2]–[4], [23] ('Equations' in Table I). In [2], [3], the GFL controller considers only the PLL and neglects the dynamics of all other control loops. As a result, the respective $k_p - SCR$ and $k_i - SCR$ stability curves of Fig. 9 match the ND-SBT outputs when the droop function is suppressed by using very high m_p, but fail to capture the true trend when m_p attains realistic values. Notably, [2] and [3] ignore the feasibility boundary by extending their curves into the infeasible region in contrast to ND-SBT.

The respective GFM models in [4], [23] employ approximations for the network and simplify control functions to reach symbolic expressions. The resulting stability misrepresentation is shown in the stability curves in Fig. 10(a)-(b) caused by ignoring the effect of k_{pv} and m_p in [23] and [4] respectively.

In conclusion, the stability assessment via "equations" in the literature may be more elegant, but entails substantial misrepresentation due to simplifications involved. ND-SBT, although

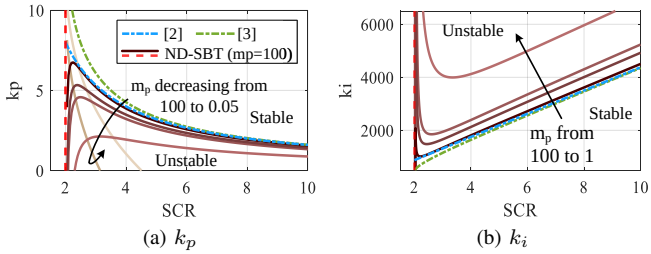

Fig. 9. (a) $k_p - SCR$ and (b) $k_i - SCR$ stability curves for GFL with varying m_p values via [2], [3] and ND-SBT.

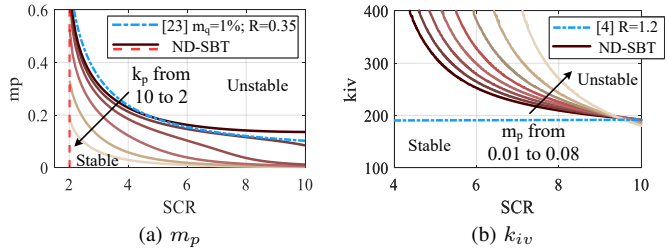

Fig. 10. (a) $m_p - SCR$ [23] and (b) $k_{iv} - SCR$ [4] stability curves for GFM from literature and ND-SBT.

an algorithm, is of pure mathematical nature throughout, thus retaining the universal applicability of equations but without compromise on accuracy.

4) GFL and GFM stability duality: Having established that the stability impact of various parameters may differ on GFL and GFM, it may be useful to superimpose the stability boundaries of both controllers on the same plot. Such an example is given in Fig. 11 for the $m_p - SCR$ relation, which reveals four distinct regions: (i) infeasible region limited by power transfer capability, (ii) stable region for GFM only, (iii) stable region for both inverters and (iv) stable region for GFL only. This region characterization enabled by ND-SBT allows for the first time visual demonstration of the two controllers' stability

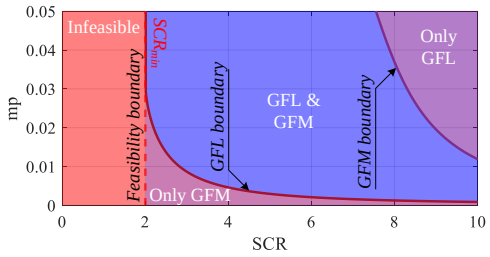

Fig. 11. Superimposed GFL and GFM $m_p - SCR$ stability curves.

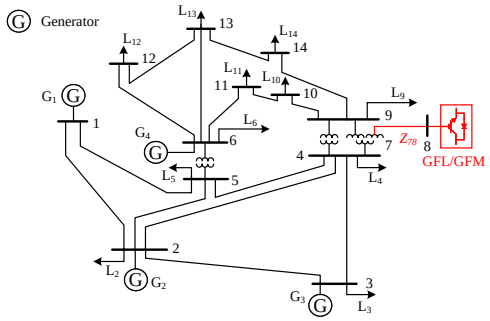

Fig. 12. Modified IEEE 14-bus testbench.

and feasible regions. Such illustrations can be quite useful when selecting the IBR controller, effectively transcending traditional 1-D criteria based solely on SCR, e.g. [36] or IEEE standards 1204-1997, to multiple dimensions.

V. IEEE 14-BUS SYSTEM RESULTS

Since ND-SBT and all methods in Table I adopt a Thévenin representation of the grid, it is important to evaluate the applicability to actual power systems. This section employs the IEEE 14-bus testbench [37] for that purpose, after replacing one generator with an IBR as shown in Fig. 12 (parameters in Table VIII). Three methods are tested here as representatives of the main approaches to stability boundary tracking: (i) exhaustive search using the full IEEE 14-bus model (*14bus-ES*), (ii) exhaustive search using Thévenin grid representation but with an LPF to break the algebraic loop (*IB-ES*), and (iii) the proposed ND-SBT algorithm. 14bus-ES refers to the conventional, detailed but complex approach, while IB-ES represents the brute-force search with a simplified model like in [17], [24], [26] from Table I. IB-ES and ND-SBT require the Thévenin equivalent of the power system as seen from node 8, easily derived as in [38]. These core literature representatives were also compared to specific equations-based symbolic boundary models from [2]–[4], [23] for completeness. The grid strength is modified by varying the impedance of line 7-8 and quantified through SCR via (24). 14bus-ES and IB-ES were implemented in MATLAB/Simulink, while equation-based models and ND-SBT were coded in MATLAB scripts with generic instructions implementable in any programming language.

A. Boundary Tracking Accuracy

1) ND-SBT versus Exhaustive Search: Fig. 13(a)-(b) depict the $m_p - SCR$ stability curves for GFL and GFM derived by the three models (continuous lines) alongside the infeasibility

TABLE VIII
IEEE 14-BUS TESTBENCH DEFAULT SETTINGS

Model	Parameter
Bus 8†	$P^* = 0.8$; $Q^* = 0.17$; $V^* = 1.09$.
GFL	$SCR = 2$; $m_p = 1\%$; $f_c = 20$ Hz; $k_p = 0.4$; $k_i = 8000$.
GFM	$SCR = 6$; $m_p = 5\%$; $f_c = 20$ Hz; $k_{pv} = 3$; $k_{iv} = 300$.

†The remaining parameters of the IEEE 14-bus system are available online at [37].

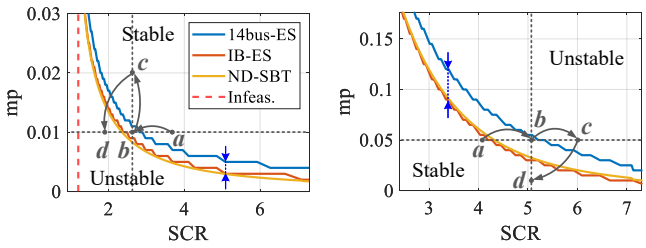

(a) GFL (b) GFM

Fig. 13. $m_p - SCR$ stability curves on the IEEE 14-bus testbench.

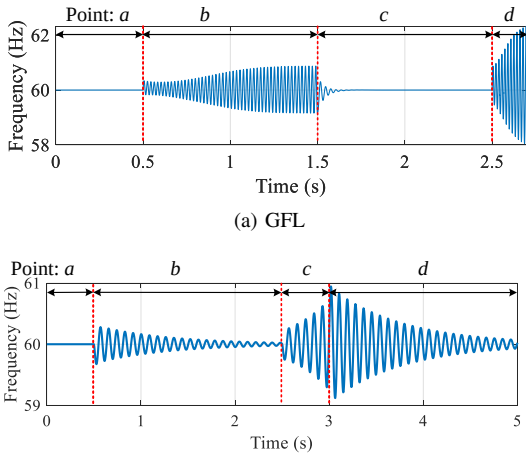

(a) GFL

(b) GFM

Fig. 14. Time-domain simulation results of the IEEE 14-bus testbench.

boundary (dashed line). A quick glance reveals that all models follow the same trend, with IB-ES (red) and ND-SBT (yellow) perfectly matching but deviating from 14bus-ES (blue). This indicates that ND-SBT is as accurate as the single-bus equivalent of the network, as shown by the blue arrows in Fig. 13, implying that some information is lost in the Thévenin representation.

To understand the importance of this misrepresentation, time-domain simulations are performed on the full IEEE 14-bus system considering operating point trajectory $a \rightarrow b \rightarrow c \rightarrow d$ as displayed in Fig. 13(a)-(b). The GFL results of Fig. 14(a) confirm valid ND-SBT classification of a (stable), c (stable) and d (unstable), but misclassification of b as stable while it turns out to have slightly negative damping. Similar findings are obtained from Fig. 14(b) for GFM, when only b is miscalculated as unstable from ND-SBT but exhibits low positive damping in reality. Although clearly miscalculations, the near-zero damping values in these cases indicate misrepresentation within a reasonable error margin.

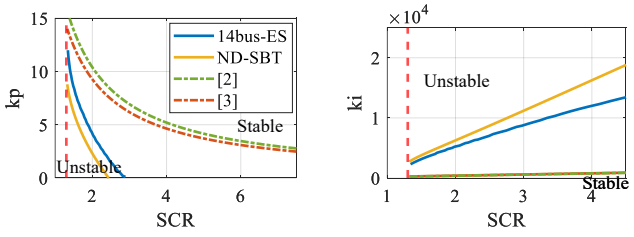

(a) k_p (b) k_i

Fig. 15. (a) $k_p - SCR$ and (b) $k_i - SCR$ stability curves for GFL in 14-bus via [2], [3], ES and ND-SBT.

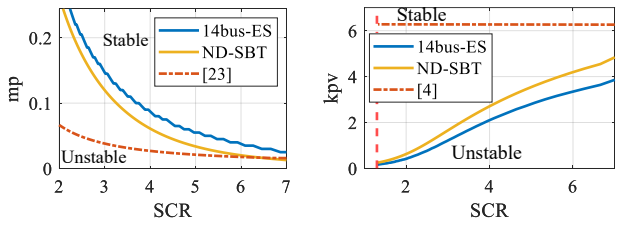

(a) m_p (b) k_{pv}

Fig. 16. (a) $m_p - SCR$ [23] and (b) $k_{pv} - SCR$ [4] stability curves for 14-bus GFM from literature, ES, and ND-SBT.

TABLE IX
IEEE 14-BUS SYSTEM 1-D BOUNDARY CALCULATION TIMES (S)

Control	Model	Parameter of interest						
		m_p	f_c	k_p/k_{pv}	k_i/k_{iv}	SCR	P^*	Q^*
GFL	14bus-ES	92	217	267	342	361	211	243
	IB-ES	55	131	156	207	308	127	138
	ND-SBT	**4.1**	**4.0**	**4.0**	**4.1**	**56.6**	**4.0**	**4.0**
GFM	14bus-ES	91	215	180	180	365	447	364
	IB-ES	53	125	105	102	306	263	214
	ND-SBT	**4.1**	**4.1**	**4.1**	**4.1**	**56.6**	**4.1**	**4.0**

2) ND-SBT versus Equations: The equations-based methods of Table I [2]–[4], [23] are also applied to the IEEE 14-bus system and compared against ND-SBT. In the case of GFL (Fig. 15), ND-SBT results are in line with 14bus-ES, although minor deviations occur due to the simplified Thévenin representation discussed earlier. In contrast, the curves from [2] and [3] exhibit significant deviations from the benchmark, particularly glaring in the $k_i - SCR$ curves, as their symbolic formulations consider only PLL dynamics and neglect all other control loops. The symbolic models in [23] and [4], which approximate the GFM network and simplify control structures, result in noticeable mismatches from ES and ND-SBT results (Fig. 16) and even fail to capture parameter-dependency effects. This analysis reaffirms that ND-SBT delivers superior fidelity in boundary-tracking and avoids misrepresenting critical trends caused by over-simplified assumptions.

B. Boundary Tracking Computation

The computational performance of the three methods is analysed here by measuring the time to derive the critical value of all parameters of interest (1-D stability boundary). The times recorded in Table IX (average values of 5 runs, lowest values in bold) reveal that ND-SBT is one to two orders of magnitude faster than the exhaustive search alternatives. Interestingly, IB-ES does not impress by only halving the 14bus-ES times at best. This substantiates the benefit from a purely mathematical formulation that avoids software-specific overheads (e.g. linear analysis in MATLAB) and the use of bisection instead of linear search. It is worth noting that the computational gain by ND-SBT in critical SCR calculation is much lower (about 6 times), as varying that parameter introduces the overhead of recalculating the Thévenin equivalent in every iteration.

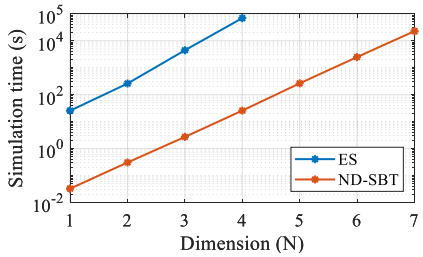

Fig. 17. ND-SBT vs ES algorithm simulation time for up to 7 dimensions.

The time savings are expected to skyrocket for larger systems and multidimensional boundaries. Fig. 17 provides the execution times of ND-SBT and ES for up to 7 dimensions (all parameters of interest); to avoid the Thévenin calculation overhead and ensure a fair comparison between the two methods, the Thévenin calculation is simplified in this test and the equivalent grid impedance is directly specified as an input similar to a single-bus system. Taking the GFL case as an example, key parameters $\{SCR, m_p, f_c, k_p, k_i, P, Q\}$ define up to 7 dimensions. Starting from the 1D stability boundary in SCR, ES exhaustively searches 40 sample points in the range $SCR \in [2, 10]$ whereas ND-SBT applies bisection. Thereafter, for higher-dimensional boundaries ($2D \rightarrow 7D$), additional parameters are introduced successively (m_p for 2D, f_c for 3D, k_p for 4D, and so on) each sampled at ten points.

Fig. 17 depicts that ND-SBT is consistently 3-4 orders of magnitude faster than ES in all dimensions. For example, the execution time of 1-D ES is roughly comparable to 4-D SBT, and 4-D ES to 7-D SBT. Both methods grow exponentially with dimension (execution time $O(N) = O(1)\, M^{N-1}$, where $O(1)$ is 1D time cost and each dimension N has M sampling points), which is why the curves appear linear in the log-scale plot. The key difference is the much smaller $O(1)$ base cost of ND-SBT, which yields a significant time-saving advantage and enables higher-dimensional analysis within practical computational limits.

Notably, while visualizing the system in higher dimensions can be challenging, graphical boundary representation is not necessary for stability assessment. The resulting envelope partitions the N-dimensional space into stable and unstable regions, enabling purely mathematical evaluation of stability under any conditions. This constitutes a standard point classification task (or point-in-region testing) in computational geometry, solvable with common methods such as the convex hull or signed distance function approximation [39], [40].

VI. Conclusion

This analysis shows that the CF-SISB model not only resolves the algebraic loop, but improves the accuracy, computational cost and numerical stability in time-domain simulations. Furthermore and more importantly, the symbolic $\boldsymbol{A}$ matrix form of the linearized model enables a purely mathematical ND-SBT algorithm that expedites boundary tracking by orders of magnitude and is as accurate as the Thévenin grid representation. The outputs of this algorithm allow visualization of stability and feasibility regions with useful insights on the impact of various parameters and the duality of GFM and GFL controllers. Simulations on single-bus and 14-bus systems validated that the proposed ND-SBT method matches the accuracy of exhaustive search while providing much higher computational efficiency and avoiding the over-simplifications of equation-based approaches. These tools can be useful when tuning parameters and grid settings, or when deciding between GFL and GFM controllers in the planning stage.

Future work is embedded application of these methods, such as real-time switching between GFL and GFM based on the extracted boundaries. Further research also involves expanding beyond the Thévenin equivalent to more elaborate representations of inverter-driven power systems and extending the ND-SBT concept to other types of stability. This will include detailed modeling of multi-inverter systems to explore control interactions between GFL and GFM units, ultimately improving the evaluation of system behavior and the assessment of stability.

Appendix

A. Solution for i_{Q0} in power flow

It is easy to show that (28) is the only acceptable solution for I_{Q0} between the two possibilities in (23) via proof by contradiction. If the solution with the "+" would hold true, then $i_{Q0} \geq e_{gD}/(2\omega_n L_g)$, which using (24) and (26) leads to

$$e_{gD} i_{Q0} \geq \frac{e_{gD}^2}{2\omega_n L_g} = \frac{SCR}{2} \geq S^* - Q^*. \tag{32}$$

However, $Q^* = -e_{gD} i_{Q0} + \omega_n L_g (i_{D0}^2 + i_{Q0}^2)$ from (21), which implies that (32) is equivalent to

$$\omega_n L_g (i_{D0}^2 + i_{Q0}^2) \geq S^*. \tag{33}$$

In physical terms, that would mean that the reactive power losses on the line impedance are higher than the inverter apparent power, which is not possible at normal conditions. Therefore, only the solution with "−" is acceptable, as in (28).

B. Symbolic $\boldsymbol{A}$ matrix

In order to calculate $\boldsymbol{A}$ matrix at a steady-state operating point x_0, one needs to first initialize the model according to Section II-B for v_{gDQ0}, i_{DQ0}, δ_0 and $\boldsymbol{x_{0,GFL}}$ or $\boldsymbol{x_{0,GFM}}$.

1) GFL model: This model employs the auxiliary variables α_{dq0} and β_{dq0} given by equations (10)-(11), the reference currents i_{dq0}^* and an auxiliary variable γ_0 used for conciseness found via

$$i_{d0}^* = \frac{P^*}{v_{gd0}},\ i_{q0}^* = -\frac{Q^*}{v_{gd0}},\ \gamma_0 = \frac{v_{gd0}}{\sqrt{(\alpha_{d0})^2 + 4\beta_{d0}}}.$$

The formulation below also employs some auxiliary partial derivatives:

$$\frac{\partial \alpha_{d0}}{\partial i_D} + j\frac{\partial \alpha_{q0}}{\partial i_D} = \frac{\partial \alpha_{q0}}{\partial i_Q} - j\frac{\partial \alpha_{d0}}{\partial i_Q} = jL_g e^{-j\delta_0} - \frac{L_g}{L_f} k_{pi} e^{-j\delta_0},$$
$$\frac{\partial \alpha_{d0}}{\partial \delta} + j\frac{\partial \alpha_{q0}}{\partial \delta} = L_g i_{dq0} - j e_{gdq0} + j\frac{L_g}{L_f} k_{pi} i_{dq0}, \frac{\partial \beta_{d0}}{\partial \Delta\omega_{filt}} = -\frac{L_g k_{pi}}{L_f m_p},$$

which are used for the partial derivatives of v_{gdq} as

$$\frac{\partial v_{gd0}}{\partial i_D} = \gamma_0 \frac{\partial \alpha_{d0}}{\partial i_D},\ \frac{\partial v_{gd0}}{\partial i_Q} = \gamma_0 \frac{\partial \alpha_{d0}}{\partial i_Q},\ \frac{\partial v_{gd0}}{\partial \delta} = \gamma_0 \frac{\partial \alpha_{d0}}{\partial \delta},$$
$$\frac{\partial v_{gd0}}{\partial \Delta\omega_{filt}} = \frac{\gamma_0}{v_{gd0}} \frac{\partial \beta_{d0}}{\partial \Delta\omega_{filt}},\ \frac{\partial v_{gd0}}{\partial \varphi_{i_d}} = \frac{L_g}{L_f}\ \gamma_0; \frac{\partial v_{gq0}}{\partial \varphi_{i_d}} = \frac{L_g}{L_f} \frac{\beta_{q0}\gamma_0}{(v_{gd0})^2},$$
$$\frac{\partial v_{gq0}}{\partial i_D} = \frac{\partial \alpha_{q0}}{\partial i_D} + \frac{\beta_{q0}\gamma_0}{(v_{gd0})^2} \frac{\partial \alpha_{d0}}{\partial i_D},\ \frac{\partial v_{gq0}}{\partial i_Q} = \frac{\partial \alpha_{q0}}{\partial i_Q} + \frac{\beta_{q0}\gamma_0}{(v_{gd0})^2} \frac{\partial \alpha_{d0}}{\partial i_Q},$$
$$\frac{\partial v_{gq0}}{\partial \delta} = \frac{\partial \alpha_{q0}}{\partial \delta} + \frac{\beta_{q0}\gamma_0}{{v_{gd0}}^2} \frac{\partial \alpha_{d0}}{\partial \delta},\ \frac{\partial v_{gq0}}{\partial \Delta\omega_{filt}} = \frac{\beta_{q0}\gamma_0}{(v_{gd0})^3} \frac{\partial \beta_{d0}}{\partial \Delta\omega_{filt}}.$$

Once these auxiliary variables are found, the non-zero elements of the 7x7 $\boldsymbol{A}$ matrix are explicitly found by

$$A_{1,1} = \frac{\omega_B}{L_g}\left(\frac{\partial v_{gd0}}{\partial i_D}\cos\delta_0 - \frac{\partial v_{gq0}}{\partial i_D}\sin\delta_0\right),$$
$$A_{1,2} = \frac{\omega_B}{L_g}\left(\frac{\partial v_{gd0}}{\partial i_Q}\cos\delta_0 - \frac{\partial v_{gq0}}{\partial i_Q}\sin\delta_0\right) + \omega_B,$$
$$A_{1,4} = \frac{\omega_B}{L_g}\left(\frac{\partial v_{gd0}}{\partial \delta}\cos\delta_0 - \frac{\partial v_{gq0}}{\partial \delta}\sin\delta_0 - v_{gQ0}\right),$$
$$A_{1,5} = \frac{\omega_B}{L_g}\left(\frac{\partial v_{gd0}}{\partial \Delta\omega_{filt}}\cos\delta_0 - \frac{\partial v_{gq0}}{\partial \Delta\omega_{filt}}\sin\delta_0\right),$$
$$A_{1,6} = \frac{\omega_B}{L_g}\left(\frac{\partial v_{gd0}}{\partial \varphi_{i_d}}\cos\delta_0 - \frac{\partial v_{gq0}}{\partial \varphi_{i_d}}\sin\delta_0\right),\ A_{1,7} = -\frac{\omega_B \sin\delta_0}{L_f};$$
$$A_{2,1} = \frac{\omega_B}{L_g}\left(\frac{\partial v_{gd0}}{\partial i_D}\sin\delta_0 + \frac{\partial v_{gq0}}{\partial i_D}\cos\delta_0\right) - \omega_B,$$
$$A_{2,2} = \frac{\omega_B}{L_g}\left(\frac{\partial v_{gd0}}{\partial i_Q}\sin\delta_0 + \frac{\partial v_{gq0}}{\partial i_Q}\cos\delta_0\right),$$
$$A_{2,4} = \frac{\omega_B}{L_g}\left(\frac{\partial v_{gd0}}{\partial \delta}\sin\delta_0 + \frac{\partial v_{gq0}}{\partial \delta}\cos\delta_0 + v_{gD0}\right),$$
$$A_{2,5} = \frac{\omega_B}{L_g}\left(\frac{\partial v_{gd0}}{\partial \Delta\omega_{filt}}\sin\delta_0 + \frac{\partial v_{gq0}}{\partial \Delta\omega_{filt}}\cos\delta_0\right),$$
$$A_{2,6} = \frac{\omega_B}{L_g}\left(\frac{\partial v_{gd0}}{\partial \varphi_{i_d}}\sin\delta_0 + \frac{\partial v_{gq0}}{\partial \varphi_{i_d}}\cos\delta_0\right),\ A_{2,7} = \frac{\omega_B \cos\delta_0}{L_f};$$
$$A_{3,1} = \frac{k_i}{\omega_B}\frac{\partial v_{gq0}}{\partial i_D},\ A_{3,2} = \frac{k_i}{\omega_B}\frac{\partial v_{gq0}}{\partial i_Q},\ A_{3,4} = \frac{k_i}{\omega_B}\frac{\partial v_{gq0}}{\partial \delta},$$
$$A_{3,5} = \frac{k_i}{\omega_B}\frac{\partial v_{gq0}}{\partial \Delta\omega_{filt}},\ A_{3,6} = \frac{k_i}{\omega_B}\frac{\partial v_{gq0}}{\partial \varphi_{i_d}},\ A_{3,7} = \frac{k_i L_g}{\omega_B L_f};$$
$$A_{4,1} = k_p\frac{\partial v_{gq0}}{\partial i_D},\ A_{4,2} = k_p\frac{\partial v_{gq0}}{\partial i_Q},\ A_{4,3} = \omega_B,\ A_{4,4} = k_p\frac{\partial v_{gq0}}{\partial \delta},$$
$$A_{4,5} = k_p\frac{\partial v_{gq0}}{\partial \Delta\omega_{filt}},\ A_{4,6} = k_p\frac{\partial v_{gq0}}{\partial \varphi_{i_d}},\ A_{4,7} = k_p\frac{L_g}{L_f};$$
$$A_{5,1} = k_p\frac{\omega_c}{\omega_B}\frac{\partial v_{gq0}}{\partial i_D},\ A_{5,2} = k_p\frac{\omega_c}{\omega_B}\frac{\partial v_{gq0}}{\partial i_Q},\ A_{5,3} = \omega_c,$$
$$A_{5,4} = k_p\frac{\omega_c}{\omega_B}\frac{\partial v_{gq0}}{\partial \delta},\ A_{5,5} = \omega_c\left(\frac{k_p}{\omega_B}\frac{\partial v_{gq0}}{\partial \Delta\omega_{filt}} - 1\right),$$
$$A_{5,6} = k_p\frac{\omega_c}{\omega_B}\frac{\partial v_{gq0}}{\partial \varphi_{i_d}},\ A_{5,7} = k_p\frac{\omega_c L_g}{\omega_B L_f},$$
$$A_{6,1} = -k_{ii}\left(\frac{i_{d0}^*}{v_{gd0}}\frac{\partial v_{gd0}}{\partial i_D} + \cos\delta_0\right),\ A_{6,2} = -k_{ii}\left(\frac{i_{d0}^*}{v_{gd0}}\frac{\partial v_{gd0}}{\partial i_Q} + \sin\delta_0\right),$$
$$A_{6,4} = -k_{ii}\left(\frac{i_{d0}^*}{v_{gd0}}\frac{\partial v_{gd0}}{\partial \delta} + i_{q0}\right),\ A_{6,5} = -k_{ii}\left(\frac{i_{d0}^*}{v_{gd0}}\frac{\partial v_{gd0}}{\partial \Delta\omega_{filt}} + \frac{1}{m_p v_{gd0}}\right),$$
$$A_{6,6} = -k_{ii}\frac{i_{d0}^*}{v_{gd0}}\frac{\partial v_{gd0}}{\partial \varphi_{i_d}};\ A_{7,1} = k_{ii}\left(\frac{-i_{q0}^*}{v_{gd0}}\frac{\partial v_{gd0}}{\partial i_D} + \sin\delta_0\right),$$
$$A_{7,2} = -k_{ii}\left(\frac{i_{q0}^*}{v_{gd0}}\frac{\partial v_{gd0}}{\partial i_Q} + \cos\delta_0\right),\ A_{7,4} = -k_{ii}\left(\frac{i_{q0}^*}{v_{gd0}}\frac{\partial v_{gd0}}{\partial \delta} - i_{d0}\right),$$
$$A_{7,5} = -k_{ii}\frac{i_{q0}^*}{v_{gd0}}\frac{\partial v_{gd0}}{\partial \Delta\omega_{filt}},\ A_{7,6} = -k_{ii}\frac{i_{q0}^*}{v_{gd0}}\frac{\partial v_{gd0}}{\partial \varphi_{i_d}}.$$

2) GFM model: In GFM, the reference voltage signals will be: $v_{gdq0}^* = v_{gdq0}$ and auxiliary partial derivatives used are given by

$$\frac{\partial v_{gd0}}{\partial i_D} = \frac{\partial v_{gq0}}{\partial i_Q} = \frac{-k_{pi}}{\frac{L_f}{L_g} + k_{pv}k_{pi}},\ \frac{\partial v_{gd0}}{\partial i_Q} = -\frac{\partial v_{gq0}}{\partial i_D} = \frac{-L_f}{\frac{L_f}{L_g} + k_{pv}k_{pi}},$$
$$\frac{\partial v_{gd0}}{\partial \delta} = -\frac{k_{pv}k_{pi}v_{gQ0}^* + k_{pi}i_{Q0}}{\frac{L_f}{L_g} + k_{pv}k_{pi}},\ \frac{\partial v_{gq0}}{\partial \delta} = \frac{k_{pv}k_{pi}v_{gD0}^* + k_{pi}i_{D0}}{\frac{L_f}{L_g} + k_{pv}k_{pi}};$$
$$\frac{\partial v_{gd0}}{\partial i_D} = \frac{\partial v_{gq0}}{\partial i_Q} = (L_f\sin\delta_0 - k_{pi}\cos\delta_0)/(\frac{L_f}{L_g} + k_{pv}k_{pi}),$$
$$\frac{\partial v_{gd0}}{\partial i_Q} = -\frac{\partial v_{gq0}}{\partial i_D} = -(L_f\cos\delta_0 + k_{pi}\sin\delta_0)/(\frac{L_f}{L_g} + k_{pv}k_{pi}),$$

$\frac{\partial v_{gd0}}{\partial \delta} = \frac{L_f i_{d0} - k_{pi} i_{q0} + \frac{L_f}{L_g} e_{gq0}}{\frac{L_f}{L_g} + k_{pv} k_{pi}}$, $\frac{\partial v_{gq0}}{\partial \delta} = \frac{L_f i_{q0} + k_{pi} i_{d0} - \frac{L_f}{L_g} e_{gd0}}{\frac{L_f}{L_g} + k_{pv} k_{pi}}$,
$\frac{\partial v_{gd0}}{\partial \varphi_{v_{gd}}} = \frac{\partial v_{gq0}}{\partial \varphi_{v_{gq}}} = \frac{k_{pi}}{\frac{L_f}{L_g} + k_{pv} k_{pi}}$, $\frac{\partial v_{gd0}}{\varphi_{i_d}} = \frac{\partial v_{gq0}}{\partial \varphi_{i_q}} = \frac{1}{\frac{L_f}{L_g} + k_{pv} k_{pi}}$.

The non-zero elements of the 8x8 $\boldsymbol{A}$ matrix will then be

$A_{1,1} = A_{2,2} = \frac{\omega_B}{L_g} \frac{\partial v_{gd0}}{\partial i_D}$, $A_{1,2} = -A_{2,1} = \frac{\omega_B}{L_g} \frac{\partial v_{gd0}}{\partial i_Q} + \omega_B$,
$A_{1,4} = \frac{\omega_B}{L_g} \frac{\partial v_{gd0}}{\partial \delta}$, $A_{2,4} = \frac{\omega_B}{L_g} \frac{\partial v_{gq0}}{\partial \delta}$,
$A_{1,5} = A_{2,6} = k_{pi} A_{1,7} = k_{pi} A_{2,8} = \frac{\omega_B}{L_g} \frac{k_{pi} \cos \delta_0}{(L_f/L_g) + k_{pv} k_{pi}}$,
$A_{1,6} = -A_{2,5} = k_{pi} A_{1,8} = -k_{pi} A_{2,7} = \frac{\omega_B}{L_g} \frac{-k_{pi} \sin \delta_0}{(L_f/L_g) + k_{pv} k_{pi}}$;
$A_{3,1} = -\omega_c \left(v_{gD0} + i_{D0} \frac{\partial v_{gd0}}{\partial i_D} + i_{Q0} \frac{\partial v_{gq0}}{\partial i_D} \right)$,
$A_{3,2} = -\omega_c \left(v_{gQ0} + i_{D0} \frac{\partial v_{gd0}}{\partial i_Q} + i_{Q0} \frac{\partial v_{gq0}}{\partial i_Q} \right)$, $A_{3,3} = -\omega_c$,
$A_{3,4} = -\omega_c \left(i_{D0} \frac{\partial v_{gd0}}{\partial \delta} + i_{Q0} \frac{\partial v_{gq0}}{\partial \delta} \right)$,
$A_{3,5} = k_{pi} A_{3,7}$, $A_{3,6} = k_{pi} A_{3,8}$,
$A_{3,7} = -\omega_c \frac{i_{d0}}{\frac{L_f}{L_g} + k_{pv} k_{pi}}$, $A_{3,8} = -\omega_c \frac{i_{q0}}{\frac{L_f}{L_g} + k_{pv} k_{pi}}$; $A_{4,3} = \omega_B m_p$;
$A_{5,1} = A_{6,2} = -k_{iv} \frac{\partial v_{gd0}}{\partial i_D}$, $A_{5,2} = -A_{6,1} = -k_{iv} \frac{\partial v_{gd0}}{\partial i_Q}$,
$A_{5,4} = -k_{iv} \frac{\partial v_{gd0}}{\partial \delta}$, $A_{6,4} = -k_{iv} \frac{\partial v_{gq0}}{\partial \delta}$,
$A_{5,5} = A_{6,6} = -k_{iv} \frac{\partial v_{gd0}}{\partial \varphi_{v_{gd}}}$, $A_{5,7} = A_{6,8} = -k_{iv} \frac{\partial v_{gd0}}{\varphi_{i_d}}$;
$A_{7,1} = A_{8,2} = -k_{ii} k_{pv} \frac{\partial v_{gd0}}{\partial i_D} - k_{ii} \cos \delta_0$,
$A_{7,2} = -A_{8,1} = -k_{ii} k_{pv} \frac{\partial v_{gd0}}{\partial i_Q} - k_{ii} \sin \delta_0$,
$A_{7,4} = -k_{ii} k_{pv} \frac{\partial v_{gd0}}{\partial \delta} - k_{ii} i_{q0}$, $A_{8,4} = -k_{ii} k_{pv} \frac{\partial v_{gq0}}{\partial \delta} + k_{ii} i_{d0}$,
$A_{7,5} = A_{8,6} = -k_{ii} k_{pv} \frac{\partial v_{gd0}}{\partial \varphi_{v_{gd}}} + k_{ii}$,
$A_{7,7} = A_{8,8} = -k_{ii} k_{pv} \frac{\partial v_{gd0}}{\varphi_{i_d}}$.

REFERENCES

[1] F. Han, X. Zhang, M. Li, F. Li, and W. Zhao, "Stability control for grid-connected inverters based on hybrid-mode of grid-following and grid-forming," *IEEE Trans. Ind. Electron.*, 2023.

[2] S. Maulik and V. John, "Synchronization stability of 3-phase grid connected inverters in weak grids," in *Proc. IECON 2022 – 48th Annu. Conf. IEEE Ind. Electron. Soc.*, 2022, pp. 1–6.

[3] J. Xu, Y. Hu, H. Qian, and S. Xie, "Delay-based phase-locked loop parameters design based on stability region of grid-connected single-phase inverter under grid voltage sags," *IEEE Trans. Ind. Electron.*, vol. 69, no. 11, pp. 11 324–11 334, 2021.

[4] M. H. Ravanji, D. B. Rathnayake, M. Z. Mansour, and B. Bahrani, "Impact of voltage-loop feedforward terms on the stability of grid-forming inverters and remedial actions," *IEEE Trans. Ind. Electron.*, vol. 38, no. 3, pp. 1554–1565, 2023.

[5] J. Li, Y. Li, and Y. Gu, "The impact of frame transformations on power system emt simulation," *IEEE Trans. Power Syst.*, vol. 39, no. 1, pp. 1319–1328, 2023.

[6] A. Safavizadeh, T. Vahabzadeh, S. Ebrahimi, and J. Jatskevich, "Admittance-based modeling of grid-following converters for time-domain simulations of multi-converter electrical power systems," in *Proc. 2023 Int. Conf. Clean Electr. Power (ICCEP)*, 2023, pp. 510–518.

[7] M. Lu, X. Wang, P. C. Loh, and F. Blaabjerg, "Resonance interaction of multiparallel grid-connected inverters with lcl filter," *IEEE Trans. Power Electron.*, vol. 32, no. 2, pp. 894–899, 2016.

[8] P. Dang *et al.*, "Dynamic interaction analysis of apf systems," *IEEE Trans. Ind. Electron.*, vol. 61, no. 9, pp. 4467–4473, 2013.

[9] L. Xiong, F. Zhuo, F. Wang, and X. o. Liu, "Static synchronous generator model: A new perspective to investigate dynamic characteristics and stability issues of grid-tied pwm inverter," *IEEE Trans. Power Electron.*, vol. 31, no. 9, pp. 6264–6280, 2015.

[10] A. Reznik, M. G. Simões, A. Al-Durra, and S. Muyeen, "LCL filter design and performance analysis for grid-interconnected systems," *IEEE Trans. Ind. Appl.*, vol. 50, no. 2, pp. 1225–1232, 2013.

[11] A. A. Adegbege and W. P. Heath, "Multivariable algebraic loops in linear anti-windup implementations," in *Proc. 2015 23rd Mediterranean Conf. Control Autom. (MED)*, 2015, pp. 514–519.

[12] N. Amiri, S. Ebrahimi, Y. Huang, and J. Jatskevich, "Improved algebraic-loop relaxation in cpvbr models of synchronous machines under power electronic switching," *IEEE Trans. Ind. Electron.*, vol. 33, no. 2, pp. 900–903, 2018.

[13] F. Therrien, M. Chapariha, and J. Jatskevich, "Pole selection procedure for explicit constant-parameter synchronous machine models," *IEEE Trans. Ind. Electron.*, vol. 29, no. 3, pp. 790–792, 2014.

[14] L. Fan, Z. Miao, and D. Ramasubramanian, "Transient algebraic impedance derivations and applications for pll-synchronized ibrs," *IEEE Trans. Power Del.*, 2023.

[15] F. Blanchini, G. Giordano, F. Riz, and L. Zaccarian, "Solving nonlinear algebraic loops arising in input-saturated feedbacks," *IEEE Trans. Autom. Control*, vol. 68, no. 4, pp. 2079–2093, 2022.

[16] J. Z. Zhou, H. Ding, S. Fan *et al.*, "Impact of short-circuit ratio and phase-locked-loop parameters on the small-signal behavior," *IEEE Trans. Power Del.*, vol. 29, no. 5, pp. 2287–2296, 2014.

[17] Z. Zou, J. Tang, X. Wang, Z. Wang, W. Chen, G. Buticchi, and M. Liserre, "Modeling and control of a two-bus system with grid-forming and grid-following converters," *IEEE J. Emerg. Sel. Topics Power Electron.*, vol. 10, no. 6, pp. 7133–7149, 2022.

[18] W. Du, Z. Chen, K. P. Schneider, R. H. Lasseter, S. P. Nandanoori, F. K. Tuffner, and S. Kundu, "A comparative study of two widely used grid-forming droop controls on microgrid small-signal stability," *IEEE J. Emerg. Sel. Topics Power Electron.*, vol. 8, no. 2, pp. 963–975, 2019.

[19] L. Ding, Y. Men, Y. Du, X. Lu, B. Chen, J. Tan, and Y. Lin, "Region-based stability analysis of resilient distribution systems with hybrid grid-forming and grid-following inverters," in *Proc. 2020 IEEE Energy Convers. Congr. Expo. (ECCE)*, 2020, pp. 3733–3740.

[20] Y. Pan, L. Chen, X. Lu, J. Wang, F. Liu, and S. Mei, "Stability region of droop-controlled distributed generation in autonomous microgrids," *IEEE Trans. Smart Grid*, vol. 10, no. 2, pp. 2288–2300, 2018.

[21] S. Eberlein and K. Rudion, "Impact of inner control loops on small-signal stability and model-order reduction of grid-forming converters," *IEEE Trans. Smart Grid*, vol. 14, no. 4, pp. 2812–2824, 2022.

[22] J. Yu *et al.*, "Evaluating small-signal synchronization stability of grid-forming converter: A geometrical approach," *IEEE Trans. Ind. Electron.*, vol. 69, no. 9, pp. 9087–9098, 2021.

[23] P. Vorobev, P.-H. Huang, M. Al Hosani, J. L. Kirtley *et al.*, "High-fidelity model order reduction for microgrids stability assessment," *IEEE Trans. Power Syst.*, vol. 33, no. 1, pp. 874–887, 2017.

[24] P. D. Achlerkar *et al.*, "Dynamic harmonic domain modeling and stability augmented design of inverter interface to weak and unbalanced grid," *IEEE Trans. Power Del.*, vol. 37, no. 4, pp. 3097–3110, 2021.

[25] M. J. Erickson *et al.*, "Improved power control bandwidth of grid-forming sources in a certs microgrid," in *Proc. 2012 IEEE Energy Convers. Congr. Expo. (ECCE)*, 2012, pp. 2366–2373.

[26] X. Luo, E. Batzelis, A. Singh, G. Saridaki, and P. Kotsampopoulos, "Stability boundary analysis of grid-forming and grid-following inverters," in *IET Conf. Proc., CP904*, vol. 2024, no. 29, 2024, pp. 245–250.

[27] Y. Tan, K. M. Muttaqi, P. Ciufo, L. Meegahapola, X. Guo, B. Chen, and H. Chen, "Enhanced frequency regulation using multilevel energy storage in remote area power supply systems," *IEEE Trans. Power Syst.*, vol. 34, no. 1, pp. 163–170, 2018.

[28] S. Karpana, E. I. Batzelis, G. Kampitsis, S. Maiti, and C. Chakraborty, "A soft-switched multi-port converter for pv/supercapacitors hybrid systems enabling frequency response services," *IEEE Trans. Ind. Appl.*, vol. 60, no. 3, pp. 4541–4556, 2024.

[29] M. N. Musarrat, M. R. Islam, K. M. Muttaqi, and D. Sutanto, "Enhanced frequency support from a pmsg-based wind energy conversion system integrated with a high temperature smes in standalone power supply systems," *IEEE Trans. Appl. Supercond.*, vol. 29, no. 2, pp. 1–6, 2018.

[30] Model linearizer. [Online]. Available: https://uk.mathworks.com/help/slcontrol/ug/modellinearizer-app.html

[31] S. B. Haley, "The generalized eigenproblem: pole-zero computation," *Proc. IEEE*, vol. 76, no. 2, pp. 103–120, 1988.

[32] H. Xing, Y. Mou, M. Fu, and Z. Lin, "Distributed bisection method for economic power dispatch in smart grid," *IEEE Trans. Power Syst.*, vol. 30, no. 6, pp. 3024–3035, 2014.

[33] J.-C. Yakoubsohn, "Numerical analysis of a bisection-exclusion method to find zeros of univariate analytic functions," *J. Complexity*, vol. 21, no. 5, pp. 652–690, 2005.

[34] D. Groß, D. Ramasubramanian, and B. Paz, "Universal input-output model of GFM functions and data-driven verification methods," National Renewable Energy Laboratory (NREL), Golden, CO (United States), Tech. Rep., 2024.

[35] Y. Tang, *Voltage stability analysis of power system*. Springer, 2021.

[36] S. Lu, Z. Xu, L. Xiao *et al.*, "Evaluation and enhancement of control strategies for vsc stations under weak grid strengths," *IEEE Trans. Power Syst.*, vol. 33, no. 2, pp. 1836–1847, 2017.
[37] IEEE 14-bus system. [Online]. Available: https://icseg.iti.illinois.edu/ieee-14-bus-system/
[38] Y. Wang, I. R. Pordanjani, W. Li, W. Xu, T. Chen, E. Vaahedi, and J. Gurney, "Voltage stability monitoring based on the concept of coupled single-port circuit," *IEEE Trans. Power Syst.*, vol. 26, no. 4, pp. 2154–2163, 2011.
[39] A. Pregelj, M. Begovic, and A. Rohatgi, "Quantitative techniques for analysis of large data sets in renewable distributed generation," *IEEE Trans. Power Syst.*, vol. 19, no. 3, pp. 1277–1285, 2004.
[40] D. Koschier, C. Deul, M. Brand, and J. Bender, "An hp-adaptive discretization algorithm for signed distance field generation," *IEEE Trans. Vis. Comput. Graph.*, vol. 23, no. 10, pp. 2208–2221, 2017.

Xi Luo (Student Member, IEEE) received the B.Eng. degree in electrical and electronic engineering from the Xi'an Jiaotong-Liverpool University, Suzhou, China, and the University of Liverpool, Liverpool, U.K., in 2019, and the M.Sc. degree in future power networks from Imperial College London, London, U.K., in 2020. She is currently pursuing the Ph.D. degree with the School of Electronics and Computer Science, University of Southampton, U.K, where she is also a Senior Research Assistant. Her research focuses on the modeling, stability analysis, and control of inverter-based resources.

Efstratios Batzelis (Senior Member, IEEE) received a Ph.D. from the National Technical University of Athens in 2016. He has been a Lecturer with the University of Southampton since April 2021 and a Research Fellow of the Royal Academy of Engineering. He is currently the Director of the Centre for Research in All-electric Future Technologies (CRAFT) and Associate Editor for the IEEE Transactions on Sustainable Energy and IEEE Journal of Emerging and Selected Topics in Industrial Electronics. From 2017 to 2019, he was an EU Marie-Curie individual fellow of photovoltaic control and integration with Imperial College London. His research interests include renewable energy technologies and distributed energy resources, mainly solar photovoltaics, power electronics control, and power system stability.

Abhinav Kumar Singh (Member, IEEE) Abhinav Kumar Singh received the Bachelor of Technology degree from the Indian Institute of Technology Delhi, India, and the Ph.D. degree from Imperial College London, U.K., in 2010 and 2015, respectively, all in electrical engineering. Since 2019, he has been a Lecturer at the University of Southampton, U.K. He received the IEEE PES Working Group Recognition Awards in 2016, 2022, and 2023 for his contributions to multiple IEEE Task Forces. He has served as an Associate Editor for IEEE Transactions on Power Systems and the Journal of Modern Power Systems and Clean Energy. His research interests include dynamic modelling, estimation, and control of modern power networks.